Bumblebees minimize control challenges by combining active and passive modes in unsteady winds

Sridhar Ravi[1][2]*, Dmitry Kolomenskiy[1]*, Thomas Engels[3][4], Kai Schneider[3], Chun Wang[2], Joern Sesterhenn[4] and Hao Liu[1]

[1]Graduate School of Engineering, Chiba University, Japan

[2]School of Aerospace Mechanical and Manufacturing Enigneering, RMIT University, Australia

[3]M2P2-CNRS & Aix-Marseille Université, 38 rue Joliot-Curie, 13451 Marseille cedex 20 France

[4]ISTA, Technische Universität Berlin, Müller-Breslau-Strasse 12, 10623 Berlin, Germany

*Equal contributions

Abstract

The natural wind environment that volant insects encounter is unsteady and highly complex, posing significant flight-control and stability challenges. Unsteady airflows can range from structured chains of discrete vortices shed in the wake of an object to fully developed chaotic turbulence. It is critical to understand the flight-control strategies insect employ to safely navigate in natural environments. We combined experiments on free flying bumblebees with high fidelity numerical simulations and lower-order modeling to identify the salient mechanics that mediate insect flight in unsteady winds. We trained bumblebees to fly upwind towards an artificial flower in a wind tunnel under steady wind and in a von Kármán street (23Hz) formed in the wake of a cylinder. The bees displayed significantly higher movement in the unsteady vortex street compared to steady winds. Correlation analysis revealed that at lower frequencies (<10Hz) in both steady and unsteady winds the bees mediated lateral movement with body roll - typical casting motion. At frequencies in unsteady winds there was a negative correlation between body roll and lateral accelerations. Numerical simulations of a bumblebee in similar conditions permitted the separation of the passive and active components of the flight trajectories. Comparison between the free-flying and 'numerical' bees revealed a novel mechanism that enables bees to passively ride out high-frequency perturbations while performing active maneuvers and corrections at lower frequencies. The capacity of maintaining stability by combining passive and active modes at different timescales provides a viable means for volant animals and machines to tackle the control challenges posed by complex airflows.

Significance

Laboratory studies of insect flight typically employ still air or steady flow; natural flows are unsteady and turbulent. This raises fundamental questions about how insects control flight in realistic environments. We used a combination of experiments on freely flying bees, high-fidelity numerical simulations and reduced order modeling to disentangle the active and passive components of the flight dynamics of bumblebees. In unsteady winds bumblebees perform active maneuvers at lower frequencies while interacting passively with wind unsteadiness at higher frequencies. Our findings reveal a novel flight-control mechanism implemented by bumblebees to cope with complex

43   winds, one that could be widespread among volant organisms and suitable for artificial
44   flying systems operating in outdoor environments.

Introduction

Volant insects are able to maintain stable flight in natural environments, despite frequently encountering unpredictable, complex airflows. While laboratory studies of insect flight typically employ steady flow, natural flows are often unsteady, containing de-stabilizing vortices and gusts over a wide range of spatial and temporal scales. These unsteady flows are generated by the interaction between wind and obstacles (1, 2), which results in chains of discrete vortices in the near wake of trees, branches and flowers, and fully developed, turbulent flow farther away.

The fact that unsteady airflow is ubiquitous in natural environments raises the fundamental question of whether insects need to actively respond to the full spectrum of unsteady flows that they experience in the natural world, or whether some of these disturbances can be handled with minimal energetic cost via passive mechanisms. Several recent studies have quantified the flight trajectories and kinematics of insects subjected to various flow perturbations, such as discrete gusts (3), von Kármán vortex streets (4, 5), or steady vortices (6). However, kinematics alone do not allow one to easily distinguish between passive body motions induced by a fluid disturbance and active, voluntary motions generated by the insect to maneuver or correct for a perturbation, particularly when the flow environment is unpredictable or unknown.

In this study, we focus on disentangling the active vs. passive components of a bumblebee's motion while flying through the unsteady, but structured, von Kármán vortex street generated behind a circular cylinder in flow. Bumblebees are ideal model organisms for studying insect flight in complex airflow, since they are relentless foragers that continue to fly in a wide range of weather conditions (7, 8). Prior work has shown that many flying animals, including bumblebees, are most sensitive to aerial disturbances along the lateral axis and rotations along the body's longitudinal axis (i.e. roll). Rolling motion and lateral translation are also critical components of voluntary maneuvering, and some insects have been shown to employ roll as the preferred means to perform rapid flight maneuvers (9, 10). We therefore chose to generate a von Kármán vortex street behind a vertical cylinder, which provides the greatest lateral and rolling perturbations (5), and chose a cylinder size (d = 25 mm) corresponding to a typical bumblebee's wing span, which produces a chain of vortices shed at a rate of 23 Hz (5). We compare the rolling and lateral flight dynamics of bumblebees flying in the vortex street to their flight in steady flow. The relative importance of active control mechanisms vs. passive dynamics could most readily be tested by varying the level of active control that an insect can employ as it flies through unsteady flow, and quantifying the resulting change in its body dynamics and flight trajectory. However, such manipulations are unfeasible in living specimens, but numerical simulations of flying insects offer a suitable alternative. Simulations that combine flapping wing aerodynamics and free-flight dynamics provide a powerful tool that allows for simultaneous manipulation of all kinematic parameters of the insect model, aerodynamic forces and torques, and the ambient flow field. These types of simulations have provided significant insight into both the fine scale flow structures that form over flapping wings and the overall dynamics of insect flight, see (11, 12) for review, but such simulations have only been performed in still air hitherto. Here, we develop a model of a flapping bumblebee flying through a von Kármán vortex street that is nominally

90　identical to the one utilized in experiments on real bees. The model accounts for flow
91　properties at all length scales in the oncoming flow and resolves the resulting lateral and
92　roll flight dynamics of the insect due to its interaction with the wind. Such high fidelity
93　simulations require extensive computational resources, and over 8192 cores and >280
94　million grid points were used in this study, the highest number that has been used to
95　resolve flapping flight to date.

96　We compare the flight trajectories and body motions of live bumblebees flying in the
97　wake of a cylinder to those of the model bee in similar flow conditions with no active
98　control, to parsimoniously estimate the role of active control and identify the control
99　strategies being implemented by flying bumblebees.

100

101　**Results**

102　**Bumblebee Flight Dynamics**

103　During free flight in both steady and unsteady flows, the flight path of the bees typically
104　consisted of large-amplitude motions at low frequencies (i.e., "casting") that combined
105　lateral translation and rolling (Fig. 1a; (5)). In unsteady flow, higher frequency
106　translational and rolling motions were superimposed on top of these low-frequency
107　casting motions (Fig. 1c, Supplementary Video 1), and earlier investigations revealed
108　that these high-frequency motions occur primarily at the 23-Hz which is the vortex
109　shedding frequency of the cylinder (5). In contrast, the lateral casting movements
110　typically occur at frequencies below 10 Hz, and this was used as the cut-off frequency
111　for examining the low- vs. high-frequency components of motion. The overall results
112　were found to be nominally insensitive to the choice of cut-off frequency, so long as it
113　was smaller than the frequency of the von Kármán street.

114　The magnitude of lateral accelerations associated with low-frequency, casting motions
115　was similar in both steady and unsteady flow (p = 0.12, Fig 2a). High-frequency motions
116　(> 10 Hz) were not observed in steady flow. However in unsteady flow, the lateral
117　accelerations associated with high-frequency motions were significantly higher than
118　those associated with casting motions ($p < 10^{-7}$, Fig. 2a). The mean absolute roll angles of
119　bees were also similar in both airflow conditions during casting (p = 0.48, Fig. 2a). The
120　absolute roll angles measured at higher frequencies in unsteady flow were significantly
121　smaller than those at lower frequencies ($p < 10^{-6}$, Fig. 2b).

122　During low-frequency casting, there was a strong, positive correlation between the
123　instantaneous roll angle of bees and their lateral acceleration (C = 0.89±0.16 in steady
124　flow, C = 0.81±0.16 in unsteady flow), and the strength of this correlation was similar in
125　steady and unsteady flow (p = 0.20). However, for higher-frequency motions in unsteady
126　flow, there was a strong, negative correlation between roll angle and lateral acceleration
127　(C = - 0.81±0.13), which was significantly different from the correlation for low-
128　frequency motion in unsteady flow ($p < 10^{-17}$, Fig. 2c).

129　Due to the high cross correlations, to estimate the relationship between roll angle and
130　lateral acceleration, we performed a linear regression between these variables, for low-

131 frequency casting motions in both flow conditions and for high-frequency motions in
132 unsteady flow (Fig. 1b, 1d, 1e). We found the slope of the regression across all flight
133 trials and compared mean values between flow conditions. For low-frequency casting
134 motions, a statistically similar, positive regression slope was present in both wind
135 conditions (p = 0.866, Fig. 2d). However, at higher frequencies in unsteady flow, the
136 slope of this relationship was negative, and significantly different from the slope for low-
137 frequency motions in unsteady flow ($p < 10^{-14}$, Fig. 2d).

Assessing the Presence of Active Flight Control

139 The high-fidelity numerical simulations were conducted to evaluate the passive flight
140 dynamics of a flapping bumblebee with no active control, flying in a von Kármán vortex
141 street with the same characteristics as the experimental unsteady flow condition. Flight
142 was simulated over 0.5 sec (76 wing beats), during which time the bumblebee
143 interacted with a number of vortices in the von Kármán street (Fig. 3, Supp. Video 2,
144 Supp. Fig. 1). The main outcome of the numerical simulation is the time evolution of the
145 aerodynamic forces and torques acting on the insect, as well as the resulting lateral and
146 rolling motions of the 'numerical' bee. Because the simulations did not include voluntary
147 low-frequency casting motions, the flight dynamics of the model bee in the simulations
148 were high-pass filtered and analyzed in the same way as the high-frequency motions of
149 real bees flying in unsteady flow.

150 The high-pass filtered lateral and rotational positions and accelerations from the
151 simulation showed good agreement with experimental measurements (Fig. 4 a - d). The
152 time-varying lateral and rolling motions were nominally within the standard deviations
153 of the high-frequency components of motion measured on freely flying bees in unsteady
154 wind, and mean values of absolute roll angle and lateral acceleration were not
155 significantly different from measurements on real bees (roll angle: p = 0.65; lateral
156 acceleration: p = 0.37).

157

Discussion

159 Aerial locomotion at small scales is very changeling and insects utilize a variety of
160 unsteady aerodynamic mechanisms to generate the necessary forces to not only stay
161 aloft but also perform coordinated maneuvers. In the natural environment volant
162 organisms are also posed with wind unsteadiness. What are the added challenges
163 imposed by wind unsteadiness and what mechanisms do insects employ to mitigate
164 them?

Low-frequency motions

166 In both steady and unsteady winds, bumblebees performed casting movements
167 consisting of large, lateral displacements at low frequencies (Fig. 1a & Supp. Video 1).
168 Such casting motions have also been observed in other insects, including wasps and
169 honeybees (13, 14). While the significance of casting is not completely understood, some
170 insects such as wasps perform casting flights to aid visual processing (13). In the
171 experiments conducted here, the high, positive cross-correlation between roll angle and

172 lateral acceleration at the low frequencies associated with casting behavior (Fig. 2c)
173 suggests a causative relationship between these motions.

174 The "helicopter model" of flight control, in which the net aerodynamic force vector
175 remains fixed relative to the body and body attitude is adjusted to alter the direction of
176 motion, has been demonstrated in several species of insects and birds (15, 16). Based on
177 this model, acceleration or deceleration along the longitudinal axis requires a change in
178 body pitch, and lateral maneuvers require a body rotation around the roll axis, to
179 reorient the aerodynamic force vector. Our data on low-frequency casting motions in
180 bumblebees supports the helicopter model of flight control. Considering level
181 translation only along the lateral axis, the relationship between body roll (ψ, in rad)
182 (refer to Supp. Fig. 1 for coordinate system) and lateral acceleration based on the
183 helicopter model is (g tan ψ) (refer S2.1 for derivation), where g is the acceleration due
184 to gravity. The roll angles observed during casting were sufficiently small, and upon
185 applying the small angle approximation, the relationship between the roll angle and
186 lateral acceleration becomes linear with the proportionality coefficient nominally equal
187 to the acceleration due to gravity (see S2.1 for derivation). In our experiments, since the
188 bees maintained altitude while casting in both steady and unsteady flow, the slope of the
189 regression line between body roll and lateral acceleration was close to the expected
190 value of 9.8 m/s^2/rad (steady airflow = 8.6 ± 1.2 m/s^2, unsteady airflow = 8.8 ± 1.5 m/s^2;
191 Fig. 2d).

192 The high correlation and positive relationship between low-frequency rolling motions
193 and lateral acceleration in both steady and unsteady winds (Fig. 2d) suggests that the
194 bees were performing the same type of controlled maneuvers at low frequencies in both
195 flow situations. Additionally, the presence of casting motions even in the absence of
196 external flow perturbations (i.e., in steady flow) indicates that these motions were most
197 likely voluntary (see Fig. 5a and Supp. Video 3 for schematic representation and
198 animation of casting motion, respectively). Based on the regression between lateral
199 acceleration and roll, bees are able to generate a lateral acceleration of around 1 m/s^2
200 (typical accelerations measured during casting) by rolling approximately 6 degrees
201 towards the direction of intended motion.

202 **High-frequency motions**

203 In the unsteady flow condition, we observed high-frequency rolling motions and lateral
204 accelerations superimposed on top of the slow casting motions, with a clear separation
205 between these two types of oscillations in terms of their temporal scale (Fig. 1c and
206 Supp. Video 1). These high-frequency oscillations in unsteady flow have previously been
207 shown to occur primarily at the vortex-shedding frequency associated with the wake of
208 the cylinder (5). The most obvious difference between the low-frequency casting
209 motions and the higher-frequency oscillations is in the phase relation between rolling
210 and lateral motion. During casting in both flow conditions, we found a strong, positive
211 correlation between roll and lateral acceleration (i.e., the bee rolls to the right and
212 accelerates to the right), whereas at higher frequencies, there is an equally strong but
213 negative correlation between these variables (Fig. 2c). The slope of the regression line
214 between lateral acceleration and roll angle is negative and much larger in magnitude for
215 the high-frequency motions (−80±17 m/s^2/rad; Fig. 2d); thus, mean lateral accelerations

216 are significantly larger and mean roll angles significantly smaller for high- vs. low-
217 frequency motions (Fig. 2). These findings suggest that the high-frequency oscillations
218 are fundamentally different from the voluntary, low-frequency casting motions.

219 The high-frequency oscillations corresponding to the vortex shedding rate could be
220 purely passive motions induced by the external airflow, or they could represent a
221 combination of passive, externally-induced motions and active, corrective maneuvers.
222 To distinguish between these hypotheses, we performed high-fidelity numerical
223 simulations based on the assumption that if the high-frequency motions were purely
224 passive, then a 'numerical' bumblebee with no flight control would exhibit similar
225 motion dynamics as measured in the experiments. The close similarity in temporal
226 patterns of lateral and rolling motions exhibited by real and simulated bumblebees over
227 several cycles of flow disturbance (approximately 20 wing beats; Fig. 4 a-d) lends
228 support to the notion that the high-frequency motions are indeed predominantly due to
229 passive interactions with vortices in the von Kármán street. This suggests that bees do
230 not actively respond to these flow perturbations on a wingbeat-by-wingbeat basis.

231 To further illustrate the mechanics of the passive, high-frequency motions that bees
232 exhibit in unsteady flow, we propose an idealized "sailboat" model. The governing
233 equations for the high-frequency motions exhibited by the insect can be derived by
234 considering a 'numerical' bumblebee subjected to a periodic lateral wind disturbance.
235 This is a reasonable comparison since the von Kármán street induces similar lateral
236 disturbances on a bee inflight. The relationship between the lateral acceleration and roll
237 angle experienced would be as follows (see S2.2 for derivation):

$$G = \frac{F_y}{m\psi} = \frac{-4\pi^2 f_v^2 I_{xx}}{\bar{L}m} \quad (Eq.\,1)$$

238 Here; G is the relation between lateral acceleration and roll angle (ψ, in rad), m is the
239 mass of the bee, F_y is the lateral acceleration, I_{xx} is the roll moment of inertia, $\bar{L}$ is the
240 moment arm, or the distance between the center of area and center of mass of the bee,
241 and f_v is the frequency of the von Kármán street. The model asserts that the force
242 induced by a lateral wind on the wings (which are located above the center of mass for
243 much of the stroke cycle), and the misalignment between the center of pressure and
244 center of mass of the body, leads to a lateral displacement and a corresponding roll, akin
245 to a sailboat rolling when subjected to a side wind (see Fig. 5b and Supplementary Video
246 4). This model preserves the phase relationship between roll angle and lateral
247 acceleration while buffeting in the experiments. By substituting parameters for the
248 "mean" bumblebee from the experiments into Eq. 1 the proportionality between the
249 lateral acceleration and the roll angle due to the wind disturbance is around -79
250 m/s^2/rad (see S2.2 for elaboration), which is comparable to that measured in the free
251 flying bees (-74 ± 13 m/s^2/rad), see Fig. 2d. In Eq. 1 the distance between the center of
252 aerodynamic pressure and center of mass critically influences the relationship, thus the
253 dynamics of the high frequency motion may differ vastly between insects.

254 **Bimodal Flight Control**

255 While foraging in the outdoor environment, flying organisms are likely to be subjected
256 to wind induced disturbances over a wide range of frequencies and scales, however the

magnitude of fluctuations over different frequencies and scales is still unclear due to lack of outdoor measurements. Nevertheless, performing active corrections for disturbances at all time scales is not only infeasible due to sensorimotor delays but also suboptimal. In this respect, it is vital to optimize the flight control system such that behaviorally relevant tasks can continue to be performed with minimal trade off. In the context of insect flight through unsteady winds, we distinguish between two distinct modes, i.e., the active and passive. Passive interactions with high frequency disturbances may be a suitable strategy since they impart relatively small net displacements that are likely to average over shorter time scales – as in this study where the high frequency displacements were smaller and tended to average over a few centiseconds, see Fig 1c & 5. Do the bees perform any corrective maneuvers when flying in the von Kármán street? The unfiltered time histories of the numerical simulations reveal that though the high frequency motions were relatively small in magnitude, the unsteady wind also introduces instabilities at lower frequencies, see SF2, and if uncorrected, these instabilities tend to increase over time. Therefore to maintain stable flight, some level of flight control is necessary but at frequencies much lower than the frequency of the von Kármán street. The von Kármán street induced disturbances at 23 Hz or 43 ms, which is within the perceptive limits and realms of sensorimotor response times of insects (3). Fruitflies subjected to mechanically induced rapid roll perturbations responded within 5 ms with active changes in wing kinematics (17). The passive response to higher frequencies disturbances noted in our experiments could be attributed to the relatively smaller magnitude of perturbations presented as well as the vast difference in organism properties. Additionally, insect responses to aerial perturbations have been shown to be context-specific whereby escape responses are mediated by specialized neural controllers that can be triggered within much smaller time scales (10).

Combination of active and passive modes in unsteady fluid environments is not uncommon in the animal kingdom. Classical experiments on fish swimming in von Kármán streets reveal a characteristic locomotion pattern knows as Kármán gaiting where fish passively comply with the vortex street resulting in a combined bending and swaying of the body (18). This passive mechanism significantly reduces sensorimotor demands however additional active stabilization is still necessary but at much longer timescales, see (19) for review. The flight trajectories of the bees here do not resemble Kármán gaiting, but the mechanism may be considered analogous. The sensorimotor basis for the implementation of such mechanisms in insects is still an open question while we have a better understanding of aquatic locomotion.

Measurements made on Kármán gaiting fish reveal relatively limited additional cost of locomotion in unsteady fluids (19) but the energetic cost of flight in steady vs unsteady wind is still unclear. However unlike in aquatic locomotion, the variations in orientation angles while maneuvering and high frequency motions inflight would result in a reduction in altitude due to the reorientation of the aerodynamic force vector. Thus apart from implementing corrections to maintain body posture in unsteady wind, an overall increase in force production may be necessary to maintain altitude. Additionally performing active corrections may impose further metabolic cost but measurements on bumblebees in rarified medium and in load-lifting tests reveal that they can increase force production with relatively limited energetic expense (20, 21). Taken together we

302 observe a novel flight control mechanism implemented by bumblebees to cope with
303 complex and unpredictable winds, a mechanism that could be widespread among volant
304 organisms and one that could be suitable for artificial miniature aerial vehicles flying in
305 outdoor environments.

306

307 **MATERIALS AND METHODS**

308 *Study specimens*

309 Bumblebees (*Bombus impatiens*) from a commercial breeder (BioBest) were maintained
310 in the lab and given continuous access to a foraging chamber, where they could feed
311 freely from an artificial flower containing linalool-scented nectar. Nominally similar
312 sized bumblebees (body length = 14 mm ± 0.5 mm, mass = 165 mg ± 10%) were selected
313 for flight experiments. The bees were placed in a transparent chamber (0.4 x 0.4 x 0.4
314 m) without access to food, for approximately two hours prior to the experiment

315 *Flight Tests*

316 All experiments were conducted in a 6 m-long, suction-type, open-return wind tunnel
317 with a 0.9 x 0.5 x 0.5 m working section. Once sufficiently starved, each bee was placed
318 in the wind tunnel (with no airflow) where it could feed from an artificial flower
319 resembling the one in the foraging chamber. Once feeding commenced, the bee was
320 allowed to feed for approximately 10 seconds, then separated from the nectar source
321 and released at the downstream end of the wind tunnel. Upon release, if the bee did not
322 fly towards the artificial flower, it was manually re-introduced to the nectar source and
323 subsequently separated. This procedure was repeated until direct flights to the nectar
324 source were observed. Once consistent behavior was established, wind was introduced
325 and bees were filmed as they flew upstream. The wind-speed was set to ~2.55 m/s,
326 which represents an intermediate cruising velocity for bumblebees (8, 22).

327 Each bee was flown in two airflow conditions, steady and unsteady. In the wind tunnel
328 with unimpeded (steady) flow, a uniform velocity profile was present across the
329 interrogation volume (< 2 % variation in mean flow speed) and turbulence intensity
330 (standard deviation/mean wind speed) was less than 1.2 %. With a cylinder (d = 25
331 mm) positioned vertically at the inlet of the test section, a von Kármán street developed
332 in the wake and vortex shedding occurred at 23 Hz, in agreement with the predicted
333 vortex shedding Strouhal number of 0.19 (23, 24). The vertical cylinder induced lateral
334 velocity fluctuations at the shedding rate over a range of ± 1.2 m/s. Refer to (5) for
335 further elaboration of flow conditions.

336 We filmed bees and quantified airflow within a specific interrogation volume (a cube
337 with side lengths of 100 mm, located 100 mm downstream from the cylinder). The
338 downstream distance was chosen to avoid the recirculating region in the near wake of
339 the cylinder and to allow the formation of a periodic von Kármán vortex street.   A total
340 of 13 bees were subjected to this assay, and paired trials in steady vs. unsteady flow
341 were obtained for each individual.

342

Kinematic reconstruction and analysis

Prior to experiments, a triangular marker was affixed to the dorsal surface of the thorax of each bee, to aid in quantifying its position and orientation during flight. The markers consisted of three black points representing the vertices of an isosceles triangle (measuring 2.7 x 2.3 mm) set upon a white background. During flight trials, bees were filmed as they flew through the interrogation volume using two Photron SA3 high-speed cameras sampling at 1000 Hz, placed above the wind tunnel at approximately 30° from the vertical. The recorded flight sequences were digitized using an open-source MATLAB-based routine, DLTdv5 (25), utilizing the automated tracking feature to localize the three black points on the triangular marker throughout each sequence. Digitization error in localizing the centroids of marker points is expected to be of the order of 1-2 pixels, which is much smaller than the mean number of pixels separating the markers (~30). The digitized position data were initially passed through a 4th-order, Butterworth, low-pass filter to remove any higher frequency errors due to the digitization process, with a cutoff frequency of 30 Hz, which is lower than the Nyquist frequency (500 Hz). For analysis of displacements at higher frequencies, the displacements were filtered using a high pass filter with 10Hz cut-off.

Instantaneous velocity and accelerations of the bees were calculated through numeric differentiation of the digitized position, see SF1 for coordinate system. The influence of flow conditions on the body orientation and rotation rates of bees was assessed by evaluating variation in roll, pitch and yaw angles of the triangular markers, using a rigid body assumption. The method detailed in (5) was used to calculate the instantaneous orientation and rotation rates of the bees, and to evaluate the errors associated with data capture and subsequent analysis. Subsequently, during analysis the lateral and rotational velocities and accelerations were separated into low (<10 Hz) and high frequency components of motion by applying a 4th order Butterworth 10-Hz low- or high-pass filter.

Numerical Modeling

The numerical method employed in this study is described in greater detail in (26, 27), and the bumblebee model has been introduced in (28). In this section we provide a short overview of the model, we refer to Supplementary Figure 1 for further elaboration. The bumblebee is approximated by three rigid elements: the body and two wings, which move with respect to each other. The characteristic size of the insect is the wing length, which is equal to R = 13.2 mm. The wings follow a prescribed periodic flapping motion with frequency f = 152 Hz. Their positional angle varies as $\Phi = 24°+115°/\sin(2\pi ft)$, the elevation with respect to the stroke plane is constant and equal to $\theta=12.55°$. The feathering angle α is equal to 70° during upstroke and -40° during downstroke, with sinusoidal variation at the reversals. The angle between the body longitudinal axis and the horizontal plane is equal to 24.5°, and the angle between the wing stroke plane and the horizontal plane is equal to 28°.

These wing kinematics ensure trimmed flight at u_∞=2.5 m/s, assuming that the body mass is 175 mg. The position of the insect varies in time according to the solid-body dynamics model (26). In this study, only two degrees of freedom are taken into account:

386   lateral displacement and roll rotation about the longitudinal axis of the body. The roll
387   moment of inertia is equal to $I_{xx}=10.92 \times 10^{-10}$ kg m^2. As with the experimental data
388   gathered from bees in unsteady flow, the calculated translational and rotational
389   positions and accelerations of the simulated bee were initially filtered using 4th order
390   Butterworth low-pass filter with cut-off frequency 30 Hz. Subsequently to isolate the
391   higher frequency motions, the data was high-pass filtered using a 4th order Butterworth
392   10 Hz high-pass filter.

393   To generate unsteady flow in the simulation, a vertical cylinder (diameter=26.4 mm, Re
394   = 4200) is placed in front of the insect, at approximately 80 mm from the insect's center
395   of mass (Fig. 3, Supplementary Fig. 1). The cylinder has a salient detail on one side in
396   order to break the symmetry of the flow. The flow is governed by the incompressible
397   Navier-Stokes equations, and the surrounding air has density ρ=1.177kg/m^3 and
398   kinematic viscosity η = 1.57x10^{-5} m^2/s. The flow domain is a rectangular channel of
399   length 132 mm, having a 105.6 x 52.8 mm cross-section. The no-slip boundary condition
400   at the surfaces of the insect and cylinder as well as the flow outlet condition, are
401   imposed using the volume penalization method (see (26, 27) for details). The penalized
402   equations are solved numerically using a Fourier pseudo-spectral method. The
403   boundary condition on the side-walls of the channel is periodic. The flow domain is
404   discretized using a uniform Cartesian grid consisting of 960 x 768 x 384 points (> 280
405   million grid points). The volume penalization parameter is equal to η=10^{-3}.   The
406   resulting simulated flow environment accurately reproduced the unsteady flow
407   environment used in experiments, with a vortex shedding rate and transient velocities
408   matching those measured in the experiments.

409   ***Statistical Analysis***

410   Statistical significance of experimental results was analyzed by performing paired t-tests
411   (n = 14 individuals in all cases) in MATLAB, between the low-frequency components of
412   flight in steady vs. unsteady flow, and between the low- and high-frequency components
413   of flight in unsteady flow. The mean lateral and rotational displacement and
414   accelerations obtained from the simulation were compared to those measured on freely
415   flying bees in the experiments by performing a one-sample t-test.
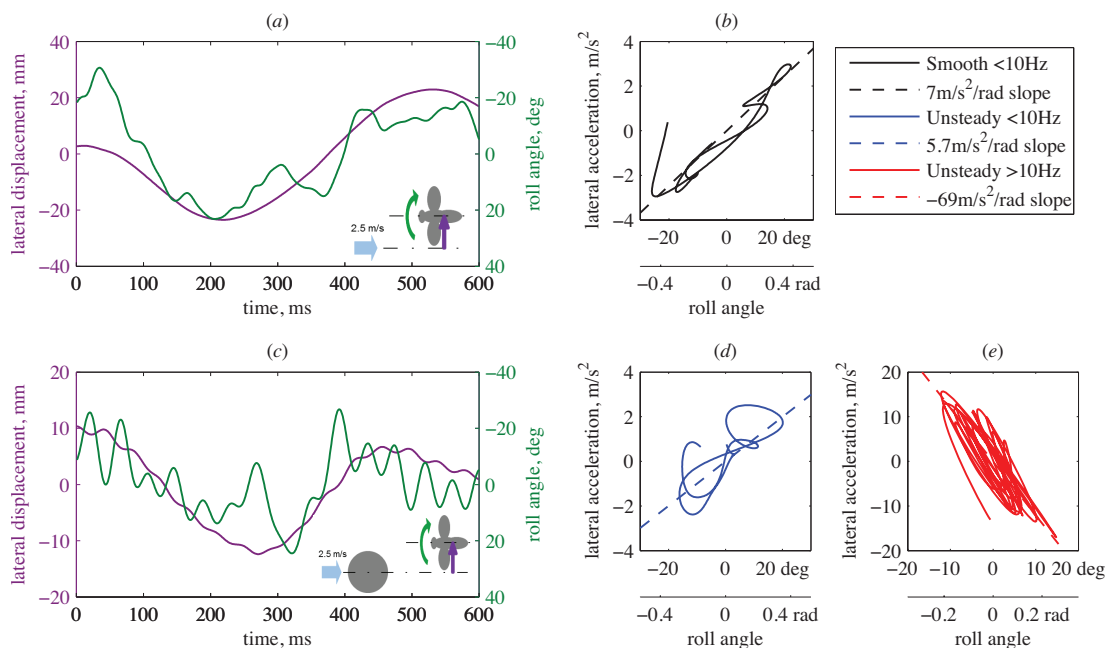
416   **References**

417   1.   Stull RB (1988) *An Introduction to Boundary Layer Meteorology* ed Stull RB
418   (Springer Netherlands, Dordrecht) doi:10.1007/978-94-009-3027-8.

419   2.   Watkins S, Milbank J, Loxton BJ, Melbourne WH (2006) Atmospheric Winds and
420   Their Implications for Microair Vehicles. *AIAA J* 44(11):2591–2600.

421   3.   Vance JT, Faruque I, Humbert JS (2013) Kinematic strategies for mitigating gust
422   perturbations in insects. *Bioinspir Biomim* 8(1):016004.

423   4.   Ortega-Jimenez VM, Greeter JSM, Mittal R, Hedrick TL (2013) Hawkmoth flight
424   stability in turbulent vortex streets. *J Exp Biol* 216(Pt 24):4567–79.

425   5.   Ravi S, Crall JD, Fisher A, Combes SA (2013) Rolling with the flow: bumblebees
426   flying in unsteady wakes. *J Exp Biol* 216(Pt 22):4299–309.

427 6.   Ortega-Jimenez VM, Mittal R, Hedrick TL (2014) Hawkmoth flight performance in
428   tornado-like whirlwind vortices. *Bioinspir Biomim* 9(2):025003.

429 7.   Crall J, Combes S (2013) Blown in the wind: Bumblebee temporal foraging
430   patterns in naturally varying wind conditions. *Integrative and Comparative*
431   *Biology* (OXFORD UNIV. PRESS INC), p E270.

432 8.   Riley JR, et al. (1999) Compensation for wind drift by bumble-bees. *Nature*
433   400(6740):126–126.

434 9.   Dudley R (2002) Mechanisms and implications of animal flight maneuverability.
435   *Integr Comp Biol* 42(1):135–40.

436 10. Muijres FT, Elzinga MJ, Melis JM, Dickinson MH (2014) Flies evade looming
437   targets by executing rapid visually directed banked turns. *Science*
438   344(6180):172–7.

439 11. Shyy W, Aono H, Kang C-K, Liu H (2013) *An Introduction to Flapping Wing*
440   *Aerodynamics* (Cambridge University Press). Volume 37 .

441 12. Sun M (2014) Insect flight dynamics: Stability and control. *Rev Mod Phys*
442   86(2):615–646.

443 13. Boeddeker N, Dittmar L, Stürzl W, Egelhaaf M (2010) The fine structure of
444   honeybee head and body yaw movements in a homing task. *Proc Biol Sci*
445   277(1689):1899–906.

446 14. Braun E, Dittmar L, Boeddeker N, Egelhaaf M (2012) Prototypical components of
447   honeybee homing flight behavior depend on the visual appearance of objects
448   surrounding the goal. *Front Behav Neurosci* 6:1.

449 15. Thomas ALR, Taylor GK (2001) Animal Flight Dynamics I. Stability in Gliding
450   Flight. *J Theor Biol* 212:399–424.

451 16. Ros IG, Bassman LC, Badger MA, Pierson AN, Biewener AA (2011) Pigeons steer
452   like helicopters and generate down- and upstroke lift during low speed turns.
453   *Proc Natl Acad Sci U S A* 108(50):19990–5.

454 17. Beatus T, Guckenheimer JM, Cohen I (2015) Controlling roll perturbations in fruit
455   flies. *J R Soc Interface* 12(105):20150075–20150075.

456 18. Liao JC, Beal DN, Lauder G V, Triantafyllou MS (2003) Fish exploiting vortices
457   decrease muscle activity. *Science* 302(5650):1566–9.

458 19. Liao JC (2007) A review of fish swimming mechanics and behaviour in altered
459   flows. *Philos Trans R Soc Lond B Biol Sci* 362(1487):1973–93.

460 20. Dillon ME, Dudley R (2014) Surpassing Mt. Everest: extreme flight performance
461   of alpine bumble-bees. *Biol Lett* 10(2):20130922.

462 21. Hedenstrom A, Ellington CP, Wolf TJ (2001) Wing wear, aerodynamics and flight
463   energetics in bumblebees (Bombus terrestris): an experimental study. *Funct Ecol*

464   15(4):417–422.

465   22.   Ellington CP (1991) Limitations on animal flight performance. *J Exp Biol* 160:71–
466   91.

467   23.   Roshko A (1961) Experiments on the flow past a circular cylinder at very high
468   Reynolds number. *J Fluid Mech* 10(03):345.

469   24.   Vickery BJ (1966) Fluctuating lift and drag on a long cylinder of square cross-
470   section in a smooth and in a turbulent stream. *J Fluid Mech* 25(03):481.

471   25.   Hedrick TL (2008) Software techniques for two- and three-dimensional
472   kinematic measurements of biological and biomimetic systems. *Bioinspir Biomim*
473   3(3):034001.

474   26.   Engels T, Kolomenskiy D, Schneider K, Sesterhenn J (2015) FluSI: A novel parallel
475   simulation tool for flapping insect flight using a Fourier method with volume
476   penalization. *arXiv* 1506.06513.

477   27.   Kolomenskiy D, Schneider K (2009) A Fourier spectral method for the Navier–
478   Stokes equations with volume penalization for moving solid obstacles. *J Comput*
479   *Phys* 228(16):5687–5709.

480   28.   Engels T, Kolomenskiy D, Schneider K, Lehmann F-O, Sesterhenn J (2016)
481   Bumblebee Flight in Heavy Turbulence. *Phys Rev Lett* 116(2):028103.

482

Figure 1: (a) Sample time series of lateral displacement and roll angle of a freely flying bumblebee in steady flow. (b) Instantaneous lateral acceleration vs. roll angle for lower-frequency (<10Hz) motions of the flight shown in (a). (c) Sample time series of lateral displacement and roll angle for the same bee flying in the

unsteady wake of a vertical cylinder. (d) Instantaneous lateral acceleration vs. roll angle for lower- (d) and higher-frequency (e) motions of the flight shown in (c). In (b), (d) and (e) the linear regression between lateral acceleration and roll angle is shown by a dashed line.
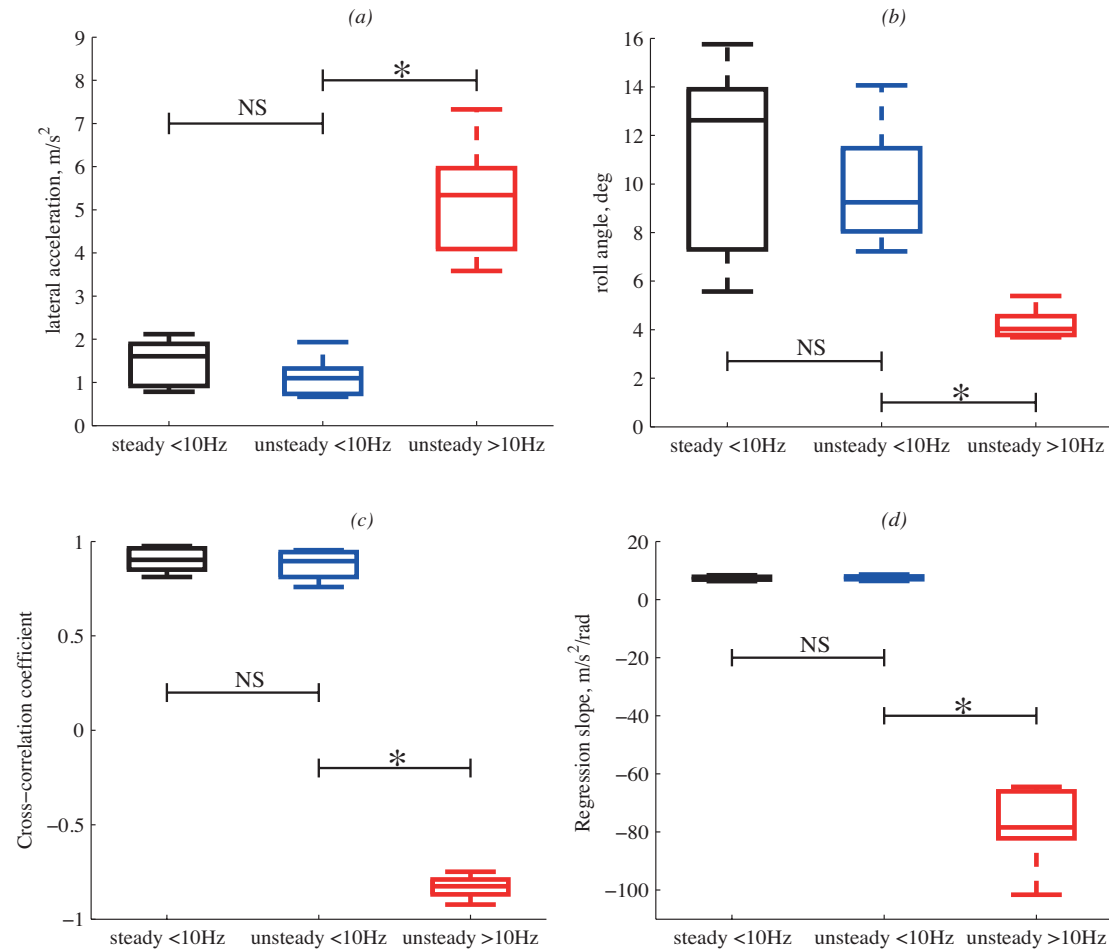

Figure 2: Mean absolute lateral acceleration (a) and (b) roll angle of lower-frequency (<10 Hz) casting motions in steady and unsteady flow, and higher-frequency (>10 Hz) motions in unsteady flow. (c) Correlation coefficients (zero time-lag, normalized cross correlation) for the relationship between instantaneous lateral acceleration and roll angle for lower-frequency (<10 Hz) casting motions in steady and unsteady flow, and higher-frequency (>10 Hz) motions in unsteady flow. (d) The slope of the regression line between lateral acceleration and roll angle, in the same flow conditions as in (c). Asterisks indicate a significant difference at the $p < 0.05$ level, n = 14 for all conditions.
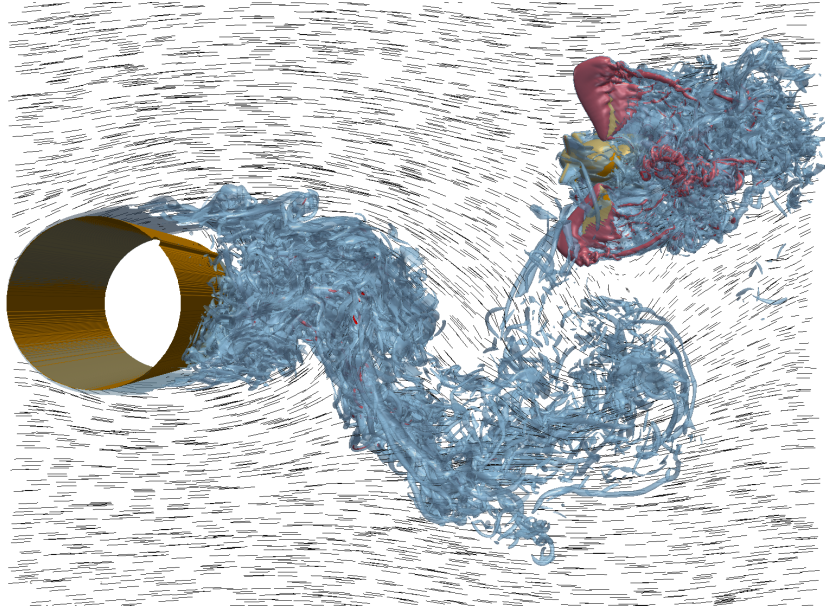
Figure 3: Birds eye view of the flow field obtained with numerical simulation. Isosurfaces of dimensionless vorticity magnitude are shown as, light blue |ω| = 5, red |ω| = 40. Arrows show the velocity in the horizontal plane that passes through the insect's center of gravity. The insect is colored in orange. Flow is shown at t = 106.5 ms after the beginning of the simulation.
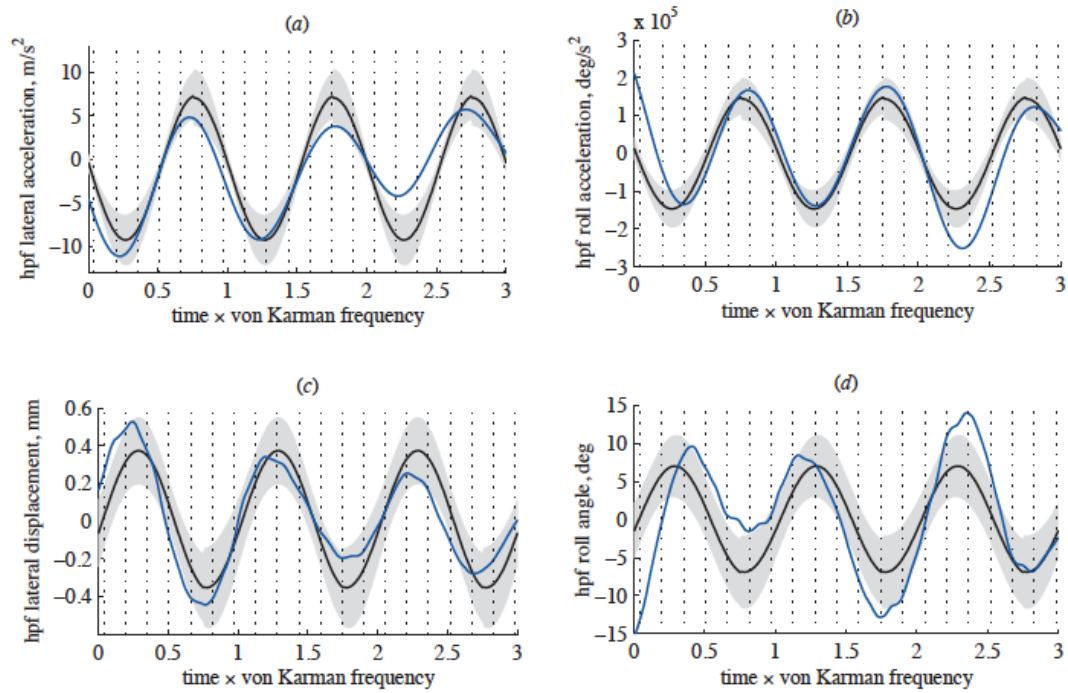

Figure 4: Time evolution of high pass filtered (hpf, > 10Hz) lateral accelerations (a) and displacements (b), and of roll accelerations (c) and angles (d) from the numerical simulation and experiments on freely flying bees. Blue line shows results of the numerical simulation (for motions > 10 Hz), and black line/gray shading

show the mean and standard deviation of measurements from experiments in unsteady flow (motions > 10 Hz). Dashed vertical lines represent wing beat periods.
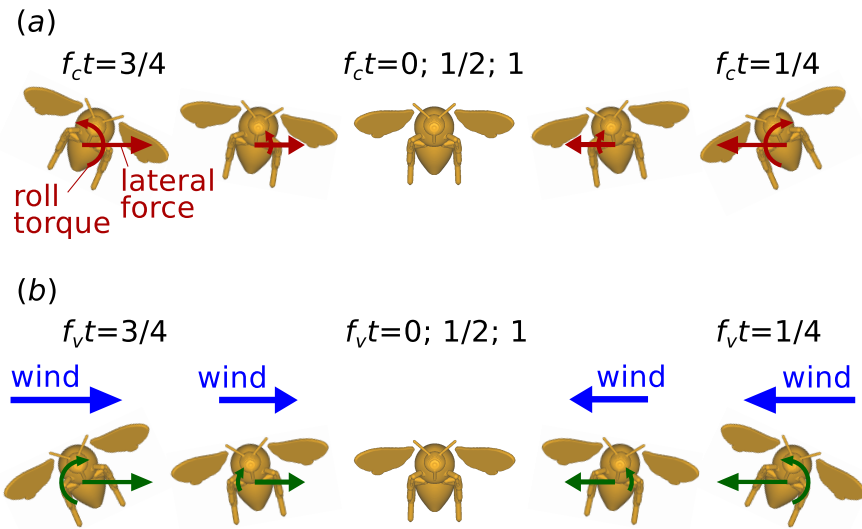

Figure 5: Schematic representation of the relationship between lateral and roll, accelerations and displacements, during (a) low frequency casting maneuvers (helicopter model) and (b) while high frequency buffeting in unsteady winds (sailboat model). The red and green arrows in (a) and (b) respectively represent the self-initiated and wind-induced forces and torques respectively. Here f_c (< 10 Hz) and f_v (≈ 23 Hz) are casting and von Kármán frequencies respectively and t is normalized time.

Supplementary material

S1   Numerical simulation

The the flow configuration used for the numerical simulation of uncontrolled flight is visualized in figure SF1, and a sample flow visualization is shown in figure 4. This section provides an extended discussion of the results of the numerical simulation.

Figure SF2 displays the time evolution of the accelerations and the displacements of the body from the beginning of the simulation. The insect in initially at rest, in-line with the cylinder, and its roll angle is zero. The asymmetry in the wake of the cylinder increases in time. The vortex street begins to have a significant influence on the insect after $t = 50$ ms.

The profiles of linear and angular accelerations are shown in figure SF2(*top row*) with blue dashed lines. They both consist of slow quasi-periodic oscillations superimposed with a high-frequency noisy component. The frequency of quasi-periodic oscillations is about 24 Hz, which is the vortex shedding frequency of the cylinder. Note that it is slightly larger in the numerical simulation than in the experiment, because the diameter of the cylinder is also larger by 5%. This acceleration is a direct consequence
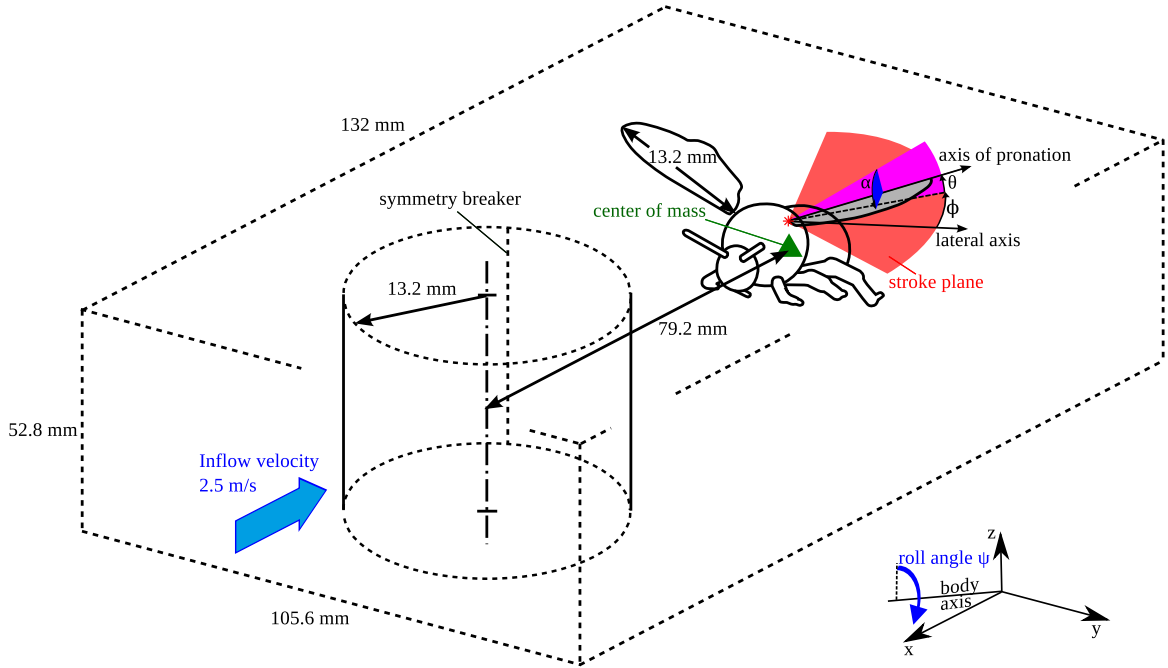
Figure SF1: Schematic drawing of the bumblebee model. See Materials and Methods section for the description of the numerical setup.

1

of the periodic sidewash by the vortex street. The high-frequency oscillations occur on the time scale even shorter than the wingbeat frequency. They are due to the aerodynamic interaction between the wings and the small-scale turbulence in the wake. In the wind tunnel experiment, the time resolution of the inverse dynamics analysis is limited by the frame rate of the video sequences. Therefore, in order to establish a comparison between the numerical simulation and the experiment, we applied the 4th order Butterworth low-pass filter at 30 Hz to the time series of the accelerations. The results are shown with the light blue lines. We focus on the time interval of three shedding periods (125 ms) after the beginning of the quasi-periodic state at $t = 95$ ms.

The time evolution of the lateral displacement and of the roll angle is shown in figure SF2(*bottom row*). Note that oscillations are only visible at the von Kármán shedding frequency and not at the flapping frequency, because time integration has a low-pass filtering effect. It is also important to keep in mind that we are considering a fluid-structure interaction problem which does not necessarily have a time-periodic solution. An impulsive start from the quescent flow initial condition and turbulence in the wake of the cylinder produce a slight imbalance between the consequent cycles of right and left sidewash during the beginning of the motion. These effects result in a slow large-amplitude drift of the insect model. However we are only interested in a time interval shorter than the slow casting motion, because the bees can definitely control their king kinematics at that long time scale. Therefore we apply the 4th order Butterworth high-pass filter at 10 Hz to the time series of lateral and angular displacement in order to focus on the quasi-periodic oscillations at the von Kármán shedding frequency. The result is shown with solid lines in figure SF2(*bottom row*). Again, we focus on a time subsequence of 125 ms to compare with the experiment.

S2   Reduced-order modeling of roll-sideslip oscillations

In this section we derive the equations that describe the dynamics of the low-frequency motion (casting) and high-frequency motion. The time series of accelerations and of the roll angle, obtained in the experiments, show scale separation between slow casting motion and rapid buffeting at the von Kármán shedding frequency. We hypothesize that these are two conceptually different modes:

- *Active (helicopter) mode*, which is a voluntary low-frequency casting motion;

- *Passive mode*, which is an unvoluntary passive high-frequency advection motion.

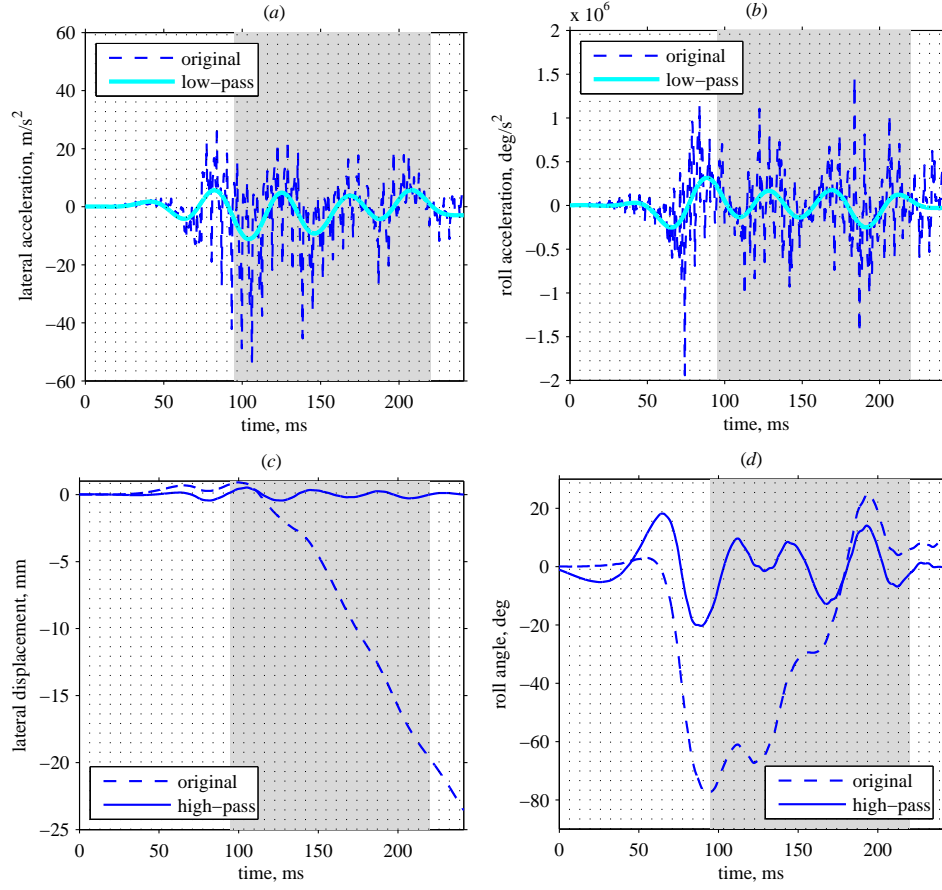We propose idealized analytical models of these two modes.

Figure SF2: Time evolution of the accelerations and displacements in the numerical simulation. Top row: lateral acceleration (a) and roll acceleration (b). Bottom row: lateral displacement (c) and roll angle (d). The gray shaded area indicates the time window used for comparison with the experiment. Vertical dotted lines indicate the wingbeat periods.
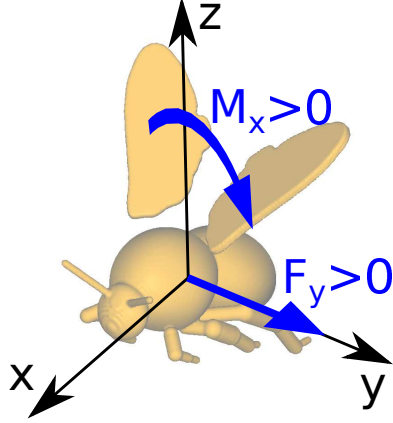
Figure SF3: Coordinate system attached to the insect body, used in the reduced-order models. Blue arrows show the positive directions of roll torque and side force.

S2.1   Active (helicopter) mode

The insect drives this motion by asymmentrically changing the kinematics of its right and left wings. Thus, the insect controls the roll moment M_x. Let us assume it varies in time as a sine wave with given frequency f_c,

$$M_x(t) = \hat{M} \sin(2\pi f_c t). \tag{1}$$

The body coordinate system is shown in figure SF3. To obtain the time evolution of the roll angle $\psi(t)$, we integrate the equation of roll motion,

$$I_{xx}\ddot{\psi} = M_x(t), \tag{2}$$

where I_{xx} is the moment of inertia. Using the time periodicity condition $\psi(t + 1/f_c) = \psi(t)$, we obtain

$$\psi = \hat{\psi} \sin(2\pi f_c t), \quad \text{where} \quad \hat{\psi} = -\frac{\hat{M}}{4\pi^2 f_c^2 I_{xx}}. \tag{3}$$

When the body roll angle ψ is non-zero, the side force F_y becomes non-zero. Let us assume that ψ varies in a range where we can use the small angle approximation (see figures 1 and 2 of the article). Since the vertical aerodynamic force supports the body weight, $F_z = mg$, we obtain

$$F_y = F_z \tan \psi \sim mg\psi. \tag{4}$$

Note that the aerodynamic force due the asymmetric wing kinematics of the right and left wings may also contribute to the lateral force. In our simple model we neglect this secondary effect. Using (3), we obtain

$$F_y = \hat{F} \sin(2\pi f_c t), \quad \text{where} \quad \hat{F} \sim -\frac{mg\hat{M}}{4\pi^2 f_c^2 I_{xx}}. \tag{5}$$

Finally, we integrate the equation of motion,

$$m\ddot{y} = F_y(t), \tag{6}$$

to obtain the time evolution of the lateral displacement,

$$y = \hat{y}\sin(2\pi f_c t), \quad \text{where} \quad \hat{y} \sim \frac{g\hat{M}}{16\pi^4 f_c^4 I_{xx}}. \tag{7}$$

The motion described by (7) and (3) is visualized in figure 6(a). Note that while $\hat{y}$ is positive, $\hat{\psi}$ is negative. This implies that the leftmost lateral position (maximum positive y) corresponds to the maximum roll to the right (maximum negative ψ). From (7) and (3) we also obtain

$$\frac{\hat{y}}{\hat{\psi}} = -\frac{g}{4\pi^2 f_c^2}. \tag{8}$$

For example, at $f_c = 2\text{Hz}$, we obtain $\hat{y}/\hat{\psi} = -62$ mm/rad. Hence, the roll amplitude of $\hat{\psi} = 20°$ would be accompanied by $\hat{y} = -22$mm lateral displacement amplitude. Whereas low-frequency casting motion only requires relatively small roll, high-frequency casting motion with the same lateral displacement amplitude would require unrealistically large roll angle.

Finally, for comparison with the experiment, it is important to notice that the gain coefficient in this model is a constant,

$$G = \frac{F_y}{m\psi} = g \approx 9.81\text{m/s}^2/\text{rad}. \tag{9}$$

S2.2 Passive mode

In this case, we suppose that the insect is only driven by the aerodynamic drag due to the external flow. A major simplifying assumption is to neglect the time variation of the shape of the insect. In addition, we assume that the roll angle is sufficiently small so that any nonlinear coupling between the lower-frequency and the high-frequency motions is negligible. The insect model is placed in a von Kármán street, which induces periodic side wind with frequency f_v. Let us assume that, in the oscillating side wind, the elementary aerodynamic force acting on a surface element $\boldsymbol{\sigma}$ at a point $\boldsymbol{\xi}$ is equal to

$$\boldsymbol{q}(\boldsymbol{\xi}, t) = \hat{\boldsymbol{q}}(\boldsymbol{\xi})\sin(2\pi f_v t). \tag{10}$$

By integration over the surface of the body, we obtain the force

$$\boldsymbol{F}(t) = \int_\Sigma \hat{\boldsymbol{q}}(\boldsymbol{\xi})\sin(2\pi f_v t)\mathrm{d}\sigma(\boldsymbol{\xi}) \tag{11}$$

and the torque

$$\boldsymbol{M}(t) = \int_\Sigma ((\boldsymbol{\xi} - \boldsymbol{x}_{cg}) \times \hat{\boldsymbol{q}}(\boldsymbol{\xi}))\sin(2\pi f_v t)\mathrm{d}\sigma(\boldsymbol{\xi}), \tag{12}$$

where Σ is the surface of the insect and $\boldsymbol{x}_{cg}$ is its center of gravity. We are only interested in the y component of $\boldsymbol{F}(t)$ and x component of $\boldsymbol{M}(t)$. Let us define the moment arm L,

$$L = M_x(t)/F_y(t). \tag{13}$$

The plus sign implies that the torque is negative if the force is positive and the center of pressure is situated above the center of gravity. We approximate L by a constant $\overline{L}$. A practical estimate of $\overline{L}$ is given later in the text. We obtain the following approximate formulae for the side force and roll torque:

$$F_y = \hat{F}\sin(2\pi f_v t), \quad \text{where} \quad \hat{F} = \int_\Sigma \hat{q}_y(\boldsymbol{\xi})\mathrm{d}\sigma(\boldsymbol{\xi}) \tag{14}$$

and

$$M_x = \hat{M}\sin(2\pi f_v t), \quad \text{where} \quad \hat{M} = \hat{F}\overline{L}. \tag{15}$$

From the solid dynamics equations (2) and (6), requiring that the motion is periodic in time, we find

$$y = \hat{y}\sin(2\pi f_v t), \quad \text{where} \quad \hat{y} = -\frac{\hat{F}}{4\pi^2 f_v^2 m} \tag{16}$$

and

$$\psi = \hat{\psi}\sin(2\pi f_v t), \quad \text{where} \quad \hat{\psi} = -\frac{\hat{F}\overline{L}}{4\pi^2 f_v^2 I_{xx}}. \tag{17}$$

This motion is visualized in figure 6(b). Note that now the sign of $\hat{y}$ is the opposite of $\hat{\psi}$. This implies that the leftmost lateral position (maximum positive y) corresponds to the maximum roll to the left (maximum negative ψ).

It is instructive to write the proportionality between the lateral displacement and the roll angle,

$$\frac{\hat{y}}{\hat{\psi}} = \frac{I_{xx}}{\overline{L}m}. \tag{18}$$

It does not depent of the frequency, in contrast to (8), but it depends on the shape of the body. In the experiments, the average body mass was equal to $m = 165$mg, moment of inertia $I_{xx} = 8.49 \cdot 10^{-10}$kgm^2, and the vortex shedding frequency $f_v = 23$Hz. The moment arm is estimated to be equal to $\overline{L} = 1.4$mm, using the numerical simulation. We thus obtain $\hat{y}/\hat{\psi} = 3.7$mm/rad. The roll angle amplitude of $20°$ corresponds now to the lateral displacement amplitude of only 1.3mm.

Finally, let us calculate the proportionality coefficient

$$\Pi = \frac{F_y}{m\psi} = -\frac{4\pi^2 f_v^2 I_{xx}}{\overline{L}m} \approx -76.6\text{m/s}^2/\text{rad}, \tag{19}$$

which is a counterpart of the gain G defined by (9).